J. Fluid Mech. (1997), *vol.* 337, *pp.* 129–153

Copyright © 1997 Cambridge University Press

Interaction of a shock with a longitudinal vortex

By G. ERLEBACHER[1], M. Y. HUSSAINI[1] AND C.-W. SHU[2]

[1]Program in Computational Science & Engineering, Florida State University, Tallahassee, FL 32306, USA

[2]Division of Applied Mathematics, Brown University, Providence, RI 02912, USA

(Received 14 April 1996 and in revised form 29 October 1996)

In this paper we study the interaction of a shock with an axisymmetric longitudinal vortex. A linearized analysis for small vortex strength is performed, and compared with results from a high-order axisymmetric shock-fitted Euler solution. It is confirmed that for weak vortices, predictions from linear theory agree well with results from nonlinear numerical simulations at the shock location. To handle very strong longitudinal vortices, which may ultimately break the shock, we use an axisymmetric high-order essentially non-oscillatory (ENO) shock-capturing scheme. Comparisons of shock-captured and shock-fitted results are performed in their regions of common validity. We also study the vortex breakdown as a function of Mach number ranging from 1.3 to 10, thus extending the range of existing results. For vortex strengths above a critical value, a triple point forms on the shock, leading to a Mach disk. This leads to a strong recirculating region downstream of the shock and a secondary shock forms to provide the necessary deceleration so that the fluid velocity can adjust to downstream subsonic conditions.

1. Introduction

Over the last 15 years, there have been numerous experimental (Dosanjh & Weeks 1965; Naumann & Hermans 1973; Délery *et al.* 1984; Cattafesta & Settles 1992; Cattafesta 1992), theoretical (Ribner 1954; Chang 1957), and computational (Pao & Salas 1981; Zang, Hussaini & Bushnell 1984; Kopriva 1988; Lasseigne, Jackson & Hussaini 1991; Meadows, Kumar & Hussaini 1991; Ellzey *et al.* 1995; Meadows 1995; Rizetta 1995; Erlebacher, Hussaini & Jackson 1996) studies of the shock–vortex interaction problem. Major effort has been devoted to investigating the interaction of a shock with either plane waves (Ribner 1954, 1986; McKenzie & Westphal 1968; Chang 1957; Erlebacher *et al*. 1996; Lasseigne *et al*. 1991) or with a vortex whose axis is aligned with the shock (Naumann & Hermans 1973; Ellzey *et al*. 1995; Erlebacher *et al*. 1996; Pao & Salas 1981; Zang *et al*. 1984). In these studies, the main interest was to understand the shock distortion, the vorticity amplification mechanisms engendered by the shock, and the properties of the radiated noise. The observations of the experiments (Naumann & Hermans 1973; Délery *et al*. 1984; Dosanjh & Weeks 1965; Cattafesta 1992) have been in general substantiated by the theoretical work of Ribner (1954, 1986), based on linear theory. Numerical simulations have recently begun to quantify some of the experimental results, in both the linear and nonlinear regimes (Meadows *et al*. 1991; Ellzey *et al*. 1995; Meadows 1995; Erlebacher *et al*. 1996).

The configuration in which the vortex has its axis normal to the shock occurs in

https://doi.org/10.1017/S0022112096004880 Published online by Cambridge University Press

practice, for example, when a wing tip vortex shed from a canard of a supersonic fighter plane intersects the shock that lies over the wing. The resulting deceleration of the vortex can lead to vortex breakdown (if the vortex and shock strengths are appropriate), resulting in destabilizing forces on the airplane (Délery *et al*. 1984). Thus, a theoretical, or heuristic determination of the conditions under which this breakdown occurs is of practical interest for both the design of fighter planes, and for the problem of controlling the resultant destabilizing forces.

There have been only a handful of experiments concerned with the longitudinal vortex/shock interaction (Cattafesta & Settles 1992; Cattafesta 1992; Délery *et al*. 1984). In these cases, particular care was taken to ensure that the vortex was axisymmetric, and that it interacted with a planar normal shock. The experiments differed in the shock creation process. For example, Cattafesta & Settles (1992) and Délery *et al*. (1984) created a shock using a two-dimensional Pitot type air intake mounted in a section of uniform flow. Cattafesta & Settles (1992) also created a normal shock wave by over-expanding the exit flow from a supersonic nozzle. The associated numerical simulations were able to reproduce the gross features of the experimental results.

To enhance our understanding of the shock-induced vortex breakdown phenomena, we study the case of a shock of infinite extent interacting with a longitudinal vortex. We find that the flow is not always steady. However, for moderately weak vortices, a steady state appears possible. The vortex breakdown is known to be a function of the helix angle which is defined as the arctangent of the ratio of the maximum azimuthal velocity and the mean axial velocity. In the incompressible case, it is observed that once the helix angle attains the critical value of 57°, the vortex is prone to breakdown (Délery *et al*. 1984; Spall, Gatski & Grosch 1987). The critical helix angle is lower for compressible flows. In the presence of a shock, the critical value of the helix angle decreases further due to the higher flow deceleration. It is attained more easily for stronger vortices and higher shock Mach numbers (Cattafesta 1992; Délery *et al*. 1984). If the vortex circulation is further increased, strong nonlinear effects come into play. The pressure associated with the vortex core, which scales quadratically with circulation, leads to nonlinear effects responsible for the formation of a Mach disk along with a strong downstream recirculating zone with a complex structure. Nonlinear effects are directly related to the product of vortex strength and shock Mach number. This is the direct result of a linear scaling of vortex strength with circulation, and a quadratic scaling of the maximum pressure variation within the vortex core.

The paper is organized as follows: §2 contains the mathematical formulation of the problem. Section 3 describes both the shock-fitted (S-F) compact difference scheme and the shock-capturing essentially non-oscillatory (ENO) method. Section 4 provides details of the linear analysis, including a simplified high-Mach-number expansion of the Rankine–Hugoniot conditions. Section 5.1 presents the consistency checks of both numerical algorithms against linear theory and against each other. In §5.2 and §5.3, we study the influence of the variation in vortex strength and shock Mach number on vortex breakdown and shock bifurcation. We first compute the vortex breakdown curve as a function of shock Mach number ranging from 1.3 to 10. Then, in §5.3, we consider vortex strengths leading to the formation of a Mach disk and strong recirculating zones downstream of the shock. Unsteady effects and the influence of initial conditions are also addressed in this section. Some concluding remarks are made in the final section.

https://doi.org/10.1017/S0022112096004880 Published online by Cambridge University Press

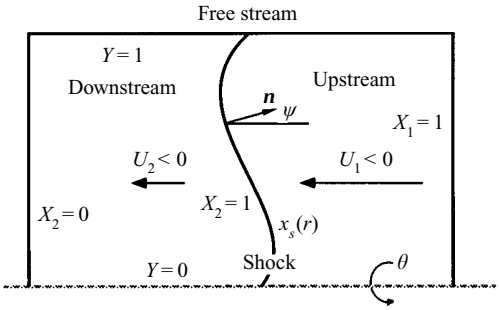


FIGURE 1. Geometry.

2. Problem formulation

We seek to study the interaction of a longitudinal vortex with a plane shock of infinite radial extent. For simplicity, the vortex is assumed to be axisymmetric with its axis perpendicular to the shock. The geometry is shown in figure 1.

The flow is assumed to be governed by the axisymmetric compressible Euler equations (in conservation form):

$$\left.\begin{aligned}
\frac{\partial \rho}{\partial t} + \frac{\partial(\rho u_x)}{\partial x} + \frac{\partial(\rho u_r)}{\partial r} + \frac{\rho u_r}{r} &= 0,\\
\frac{\partial(\rho u_x)}{\partial t} + \frac{\partial(\rho u_x^2 + p)}{\partial x} + \frac{\partial(\rho u_x u_r)}{\partial r} + \frac{\rho u_x u_r}{r} &= 0,\\
\frac{\partial(\rho u_r)}{\partial t} + \frac{\partial(\rho u_r u_x)}{\partial x} + \frac{\partial(\rho u_r^2 + p)}{\partial r} + \frac{\rho(u_r^2 - u_\theta^2)}{r} &= 0,\\
\frac{\partial(\rho u_\theta)}{\partial t} + \frac{\partial(\rho u_\theta u_x)}{\partial x} + \frac{\partial(\rho u_\theta u_r)}{\partial r} + \frac{2\rho u_\theta u_r}{r} &= 0,\\
\frac{\partial E}{\partial t} + \frac{\partial(u_x(E+p))}{\partial x} + \frac{\partial(u_r(E+p))}{\partial r} + \frac{u_r(E+p)}{r} &= 0,
\end{aligned}\right\} \tag{2.1}$$

where ρ is the density, (u_x, u_r, u_θ) are the velocity components in the axial, radial, and azimuthal directions, and E is the total energy,

$$E = \frac{p}{\gamma - 1} + \tfrac{1}{2}\rho(u_x^2 + u_r^2 + u_\theta^2), \tag{2.2}$$

with the ratio of specific heats $\gamma = 1.4$ for air. The pressure, density, and temperature are non-dimensionalized with respect to their mean upstream values P_1, ρ_1, and T_1 respectively and are related by the ideal gas law

$$p = \rho T. \tag{2.3}$$

The velocity is scaled by the reference velocity $c^* = {T_1}^{1/2}$, related to the upstream mean sound speed $c_1 = \gamma^{1/2} c^*$. In the frame of reference in which the mean shock is stationary, the mean upstream Mach number is therefore $M_1 = |U_1|/\gamma^{1/2}$, where M_1 is the upstream Mach number in a frame of reference in which the mean shock is stationary. Note that the chosen non-dimensionalization leaves the Euler equations (2.1) invariant. Finally, lengths are scaled by the vortex core radius r_0, and time is scaled by r_0/c_1^*.

The shock is initially located at the $x = 0$ plane; the axial extent of the upstream domain extends to $x = b$, while the leftmost boundary on the downstream side is

https://doi.org/10.1017/S0022112096004880 Published online by Cambridge University Press

located at $x = a$. The flow is from right to left so that $a < 0$, and $b > 0$. The axis of symmetry is $r = 0$, and the radial coordinate extends to $r = c$, where c is sufficiently large that all flow disturbances effectively vanish at this free-stream boundary.

At $t = 0$, we choose a mean flow consistent with a stationary shock at $x = 0$. Upstream of the shock ($x > 0$)

$$\rho = 1, \qquad u_x = U_1 = -\gamma^{1/2} M_1, \qquad u_r = u_\theta = 0, \qquad p = P_1 = 1, \tag{2.4}$$

while the downstream mean solution is ($x < 0$)

$$\left.\begin{aligned} &\rho = \frac{(\gamma+1)M_1^2}{(\gamma-1)M_1^2+2}, && u_x = U_2 = -\frac{\gamma^{1/2}((\gamma-1)M_1^2+2)}{(\gamma+1)M_1}, \\ &u_r = u_\theta = 0, && p = P_2 = \frac{2\gamma M_1^2 - (\gamma-1)}{\gamma+1}. \end{aligned}\right\} \tag{2.5}$$

Next, we superimpose on the mean flow an isentropic vortex with its axis along $r = 0$. Analytical forms of such vortices which are steady-state solutions of the Euler equations exist with arbitrary radial profiles. We choose an exponentially decaying profile to reduce interactions of the vortex with the outer domain boundary in the radial direction. The perturbations of azimuthal velocity u'_θ and temperature T' associated with the vortex are given by

$$u'_\theta = \frac{\epsilon r}{2\pi} \mathrm{e}^{0.5(1-r^2)} \qquad T' = -\frac{(\gamma-1)\epsilon^2}{8\gamma\pi^2 r_0^2} \mathrm{e}^{1-r^2}, \tag{2.6}$$

where r_0 is the vortex core radius and ϵ is a non-dimensional circulation at $r = 1$, related to the dimensional circulation Γ by

$$\epsilon = \frac{\Gamma}{r_0 c^*}. \tag{2.7}$$

The axial and radial velocities u'_x, u'_r are zero, the perturbation entropy $S' = \log(p/\rho^\gamma)$ is constant inside the vortex, and u'_θ is maximum at $r = 1$. Because of the particular radial profile of u'_θ, the vortex circulation decays exponentially fast to zero as $r \to \infty$. Another measure of the relative strength of the vortex is given by the ratio of the maximum u'_θ to U_1. This quantity, denoted by τ, measures the inclination of the streamlines with respect to the symmetry axis of the vortex (Délery *et al*. 1984). It is also the tangent of the helix angle. The relationship between ϵ and τ is

$$\tau = \frac{\epsilon}{2\pi M_1 \gamma^{1/2}}. \tag{2.8}$$

The upstream vortex defined by (2.6) has the following features:

(i) it is a steady-state solution of the Euler equation (2.1) if $u_x = 0$, otherwise it is passively convected by the flow with constant velocity U_1;

(ii) it has constant entropy;

(iii) there is no singularity at the symmetry axis;

(iv) it decays exponentially fast as $r \to \infty$, thus ensuring that free-stream boundary effects are virtually absent. In fact, in most calculations we set the computational boundary at $r = 5$, at which the relative effect of the perturbation on the pressure and density is of the order of 10^{-10}.

Previous studies (Cattafesta 1992; Délery *et al*. 1984) have indicated that for low and moderate vortex strengths, a steady state is eventually reached. However, the shocks in these simulations were kept stationary by either placing the shock in a

https://doi.org/10.1017/S0022112096004880 Published online by Cambridge University Press

divergent nozzle (Délery *et al*. 1984), or by attaching a Mach disk at the end of an underexpanded jet (Cattafesta 1992). Such artifacts accelerate convergence to a steady state. Should a steady state exist, one often assumes that the final state is independent of initial conditions. For example, Délery *et al*. (1984) assume that the total enthalpy is independent of time. They therefore simplify their calculations by building this constraint into the equations of motion. However, this precludes even genuinely unsteady solutions. In contrast, we do not presume that steady solutions exist. Instead, we use high-order time-dependent numerical algorithms to compute the solution which are sometimes unsteady.

To lessen possible transients during the initial stages of the simulation, we multiply the initial conditions by a function $s(x)$. We have considered three different functions:

IC-a

$$s(x) = 1.0, \tag{2.9}$$

IC-b

$$s(x) = \begin{cases} 0, & x \leqslant 0 \\ 1, & x > 0, \end{cases} \tag{2.10}$$

IC-c

$$s(x) = \begin{cases} 0, & x < \alpha \\ 1 - \left(1 - \left(\dfrac{x-\alpha}{\beta-\alpha}\right)^3\right)^3, & \alpha \leqslant x \leqslant \beta \\ 1, & x > \beta. \end{cases} \tag{2.11}$$

In case IC-a, the vortex structure (defined by u'_θ and T') is independent of the axial location and exists across both upstream and downstream domains. A shock is then externally generated along $x = 0$ at $t = 0$. The initial conditions satisfy the steady-state Euler equations, but the pressure and density jumps across the initial shock do not satisfy the steady Rankine–Hugoniot conditions (which then cause the shock to adjust itself). In case IC-b, the vortex is only defined in the upstream domain and abruptly ends at the shock, which offers a clean model configuration. Finally, case IC-c is intermediate between the first two cases. The transition function smoothly varies from zero to one and is only non-zero in the upstream domain. Thus, the Rankine–Hugoniot conditions are initially satisfied, but the upstream *modified* vortex is no longer a solution to the steady-state Euler equations. Note that IC-b is a special case of IC-c where $\alpha \to 0$, $\beta \to 0$. Numerical simulations presented in a later section will show that IC-b and IC-c actually produce similar transient structures, albeit shifted in time.

The boundary conditions are chosen as follows. We prescribe all variables at the supersonic inflow on the upstream side ($x = b$). At the subsonic downstream boundary, we employ the characteristic boundary conditions for the ENO method, or a buffer domain technique for the S-F method. The details of the buffer domain are discussed in §3. The free-stream boundary ($r = c$) is sufficiently removed from the vortex so that a simple Neumann boundary condition is sufficient for the ENO algorithm. The S-F algorithm permits a choice between characteristic conditions and Dirichlet boundary conditions (i.e. zero perturbation) in the free-stream. They both give similar results because the boundaries are sufficiently far from the vortex axis that the perturbations do not reach it during the numerical simulation. Naturally, we impose symmetry conditions at $r = 0$. Radial derivatives of all variables are set to zero, except for the azimuthal and radial velocities which vanish.

https://doi.org/10.1017/S0022112096004880 Published online by Cambridge University Press

3. Numerical methods

We adopt two numerical algorithms of high-order accuracy to solve the unsteady axisymmetric compressible Euler equations for the shock/vortex interaction problem: (i) a shock-fitted (S-F) algorithm and (ii) an essentially non-oscillatory (ENO) algorithm which captures the shock. The former is based on a sixth-order compact scheme and has the advantage of precluding Gibb's phenomena associated with shock capturing; however, its disadvantage is that it cannot handle very weak shocks or situations of strong shocks with triple points. The latter is based on adaptive stencil interpolation and nonlinearly stable time discretization, which ensures formally third-order accuracy in the smooth part of the solution while maintaining sharp essentially non-oscillatory shock transitions.

3.1. *Shock-fitting method*

The shock-fitted code solves the Euler equation in the non-conservation form

$$\frac{\partial \boldsymbol{u}}{\partial t} = -T\nabla\mathscr{P} - \boldsymbol{u}\cdot\nabla\boldsymbol{u} = \boldsymbol{R}_{\boldsymbol{u}}, \tag{3.1}$$

$$\frac{\partial \mathscr{P}}{\partial t} = -\gamma\nabla\cdot\boldsymbol{u} - \boldsymbol{u}\cdot\mathscr{P} = \boldsymbol{R}_{\mathscr{P}}, \tag{3.2}$$

$$\frac{\partial s}{\partial t} = -\boldsymbol{u}\cdot\nabla s, \tag{3.3}$$

where $s = \mathscr{P} - \gamma\log\rho$ is the entropy and $\mathscr{P} = \log p$ is the logarithmic pressure. The functions $\boldsymbol{R}_{\boldsymbol{u}}$ and $R_{\mathscr{P}}$ are the residuals of the momentum and pressure equations.

After mapping of the downstream physical domain to the computational space $X \in [0,1]$, $Y \in [0,1]$, the downstream exit becomes $X = 0$, the shock is $X = 1$, $Y = 0$ is the symmetry axis and $Y = 1$ is the free-stream boundary. All spatial derivatives are computed in computational space with a compact sixth-order discretization scheme which is stable for Dirichlet boundary conditions. Both x- and r-coordinate directions are non-periodic. Derivatives at the first and second points at both ends of the computational domain are explicitly defined by

$$hu'_0 = \sum_{i=0}^{7} a_i u_i, \quad hu'_1 = \sum_{i=0}^{7} b_i u_i,$$

where the parameters a_i and b_i are given by

$$a_i = \left\{-\frac{296}{105}, \frac{415}{48}, -\frac{125}{8}, \frac{985}{48}, -\frac{215}{12}, \frac{791}{80}, -\frac{25}{8}, \frac{145}{336}\right\}, \tag{3.4}$$

$$b_i = \left\{-\frac{3}{16}, -\frac{211}{180}, \frac{109}{48}, -\frac{35}{24}, \frac{115}{144}, -\frac{1}{3}, \frac{23}{240}, -\frac{1}{72}\right\}, \tag{3.5}$$

and h is the uniform grid spacing in computational space. Identical explicit formulae are derived for u'_N and u'_{N-1}, where N is the number of grid points along the non-periodic direction. This stencil is commonly referred to as $5^2 - 6 - 5^2$. Alternative boundary stencils are given in Carpenter, Gottlieb & Abarbanel (1993). The deriva-

https://doi.org/10.1017/S0022112096004880 Published online by Cambridge University Press

tives at interior nodes ($i = 1, \cdots, N-1$) are computed via the standard scheme (Lele 1992)

$$\sum_{j=-1}^{1} \alpha_j u'_{i+j} = h^{-1} \sum_{j=-2}^{2} \beta_j u_{i+j} \tag{3.6}$$

with coefficients $\alpha_{\pm 1} = 1$, $\alpha_0 = 3$, $\beta_{\pm 2} = 1/12$, $\beta_{\pm 1} = 7/3$ and $\beta_0 = 0$.

To maintain the sixth-order accuracy of derivatives in the radial direction at the axis, we build the required symmetry properties into the matrix derivative operator. This requires modifying the formulae for the first two radial points which are now solved as part of the implicit system. Let u_j be the value of any variable at the jth radial point, with $j = 0$ corresponding to the symmetry axis. Symmetry conditions imply that $u_{-j} = u_j$, while antisymmetric conditions imply $u_{-j} = -u_j$. Combining these requirements with the interior formula 3.6, we obtain for the point on the axis under symmetric conditions, $\alpha_0 = 3$, $\alpha_1 = 0$, $\beta_i = 0$. The first point off the axis has $\beta_2 = -\beta_0 = 7/3$, $\beta_3 = -\beta_1 = 1/12$, while the α take the interior values for the first point off the axis. The requirement of antisymmetry leads to $\alpha_0 = 3$, $\alpha_1 = 2$, $\beta_0 = 0$, $\beta_1 = 14/3$, $\beta_2 = 1/6$, $\beta_3 = 0$ for the axis point, while $\beta_1 = -\beta_{-1} = 7/3$, $\beta_0 = \beta_2 = 1/12$, and once again, the α take the interior values for the first point off the axis.

The symmetry axis is a geometric singularity, and requires special treatment. Being interior to the physical domain, the flow variables at the axis satisfy the equations of motion. Singular terms at the axis are evaluated using L'Hospital's rule. For example, u_r/r is replaced by $\partial u_r/\partial r$.

The grid is stretched in the radial direction according to

$$r = r_0 \left(\frac{\sinh (Y - Y_0)\beta}{\sinh \beta Y_0} + 1 \right), \tag{3.7}$$

where

$$Y_0 = \frac{1}{2A} \log \frac{1 + (\mathrm{e}^A - 1)(r_0/r_{max})}{1 + (\mathrm{e}^{-A} - 1)(r_0/r_{max})} \tag{3.8}$$

and $0 < Y < 1$ is the computational coordinate in the radial direction. This choice of stretching allows the grid points to concentrate around $r = 1$ and extend to a maximum radius of r_{max}; the stretching of the grid is controlled by the parameter A. As detailed in Erlebacher *et al.* (1996) we transform the downstream physical axial coordinate x using the coordinate transformation

$$X = \frac{x - a}{x_s(r, t) - a} \tag{3.9}$$

where $x_s(r, t)$ is the shock shape and $x = a$ is the leftmost boundary of the downstream domain.

At the downstream boundary, we implement the buffer domain technique introduced by Ta'assan & Nark (1995). We modify the downstream Euler equations in a finite buffer domain abutting the downstream boundary, replacing $\partial/\partial t$ by $\partial/\partial t + U_0(X)\nabla$, to control the direction of the characteristics and the characteristic speeds. At the exit plane, $X = 0$, the characteristic speeds become $u_2(b) + U_0(b)$, $U_0(b) + U_0(b) \pm c_2(b)$. The axial profile for $U_0(x)$ is a power function of degree 2. Subscripts 1 and 2 refer to upstream and downstream variables respectively.

We briefly present the derivation of a time evolution equation for the shock motion (Hussaini *et al.* 1985; Canuto *et al.* 1987; Kopriva, Zang & Hussaini 1991). Given the shock shape, $x = x_s(r, t)$, and the Euler equations, the characteristic normal to the

https://doi.org/10.1017/S0022112096004880 Published online by Cambridge University Press

shock pointing in the upstream direction has the form

$$(p_{,t} - R_p) + \zeta\, \boldsymbol{n}\cdot(\boldsymbol{u}_{,t} - \boldsymbol{R_u}) = 0 \tag{3.10}$$

where $\zeta = (\gamma/T_2)^{1/2}$ is a function of the downstream temperature and density, and $\boldsymbol{n}$ is the unit normal to the shock pointing in the upstream direction:

$$\boldsymbol{n} = \left(\frac{1}{1 + x_{s,r}^{2\ 1/2}}, \frac{-x_{s,r}}{1 + x_{s,r}^{2\ 1/2}} \right). \tag{3.11}$$

$\boldsymbol{R_u}$ and R_p are numerically computed as part of the Runga–Kutta advancement. To apply (3.10) at the shock requires the time derivatives of pressure and velocity. These are obtained by solving the Rankine–Hugoniot conditions for the downstream pressure p_2 and velocity u_2:

$$p_2 = \frac{2}{\gamma+1}\left(\frac{\gamma-1}{2}\, p_1 + \rho_1 \delta_1^2\right), \quad \delta_2 = \frac{\gamma-1}{\gamma+1}\,\delta_1 + \frac{2\gamma}{\gamma+1}\,\frac{p_1}{\rho_1 \delta_1}, \tag{3.12}$$

and differentiating (p_2, δ_2) with respect to time. Here, $\delta_i = \boldsymbol{u}_i \cdot \boldsymbol{n} - u_s$, where $u_s = w_s \hat{\boldsymbol{x}} \cdot \boldsymbol{n}$ is the shock velocity normal to the shock, while $\hat{\boldsymbol{x}}$ and $w_s = x_{s,t}$ are the unit vector and the instantaneous shock velocity respectively. The required time derivatives are readily computed and inserted into the characteristic equation above to obtain the final evolution equation

$$(n_x w_s)_{,t} = \frac{(F - \zeta A)(\boldsymbol{n}\cdot\boldsymbol{u}_1)_{,t} + \zeta\,(\boldsymbol{u}_2 \cdot \boldsymbol{n}_{,t}) + (D - \zeta B)\, p_{1,t} + (E - \delta C)\, \rho_{1,t} - \mathscr{R}}{F + \zeta(1 - A)}, \tag{3.13}$$

where

$$\mathscr{R} = R_p - \zeta\, \boldsymbol{n}_{,t} \cdot \boldsymbol{R_u} \tag{3.14}$$

and the constants A, F, D, B, E, C are functions of the upstream flow variables and the shock velocity.

Time advancement is based on a low-storage, five-stage fourth-order-accurate Runga–Kutta scheme (Carpenter & Kennedy 1994). Although 5/3 more expensive than Williamson's third-order low-storage scheme at fixed CFL, the achievable CFL is higher by a factor of 1.9, which is greater than 5/3, so with no change in memory requirement there is a net gain of CPU time, along with the increased accuracy. The interior equations and shock motion equations are advanced simultaneously in time. The Rankine–Hugoniot conditions are applied at the end of each Runga–Kutta stage to update the downstream variables at the shock.

3.2. *Shock-capturing method*

The shock-capturing method we use in this work belongs to the class of high-order nonlinearly stable essentially non-oscillatory (ENO) methods developed by Shu & Osher (1988, 1989), and Shu *et al.* (1992). The detailed description of the algorithm, along with information on efficient implementation can be found in these references. Here we only highlight a few key points and describe issues which relate to the applications of ENO schemes to the particular system of equations 2.1.

The main idea underlying an ENO scheme lies at the approximation (interpolation) level. For piecewise smooth functions and a fixed stencil, high-order interpolation schemes inevitably cross the discontinuities, causing not only loss of accuracy but also over- and under-shoots (Gibbs phenomenon). ENO (Harten *et al.* 1987) is an adaptive stencil interpolation, with the local stencil chosen as the smoothest possible

https://doi.org/10.1017/S0022112096004880 Published online by Cambridge University Press

among all candidates. This, together with upwinding (realized through flux splitting), characteristic decomposition (which effectively decouples the system locally) and a nonlinearly stable time discretization, ensures that the scheme achieves high-order resolution in the smooth part of the solution while maintaining sharp, non-oscillatory shock transitions. For the shock–vortex interaction problem considered in this paper, which contains both strong shocks and complex structures in the smooth part of the solution, a high-order ENO scheme is an ideal candidate. We use the uniformly third-order ENO scheme (fourth-order in L_1), based on a Lax–Friedrichs building block, and a third-order total-variation-diminishing Runge–Kutta time discretization (Shu *et al*. 1992).

The procedure underlying ENO schemes is best described with reference to the one-dimensional scalar version of (2.1):

$$\frac{\partial u}{\partial t} + \frac{\partial f(u)}{\partial x} = 0, \tag{3.15}$$

followed by an indication of how it can be generalized to solve the full system 2.1. The spatial derivative in 3.15 is discretized by the conservation difference approximation

$$\frac{\partial f(u)}{\partial x} \approx \frac{1}{\Delta x}\left(\hat{f}_{j+1/2} - \hat{f}_{j-1/2}\right). \tag{3.16}$$

A linear combination of the point values of the flux function $f(u)$,

$$\hat{f}_{j+1/2} = \sum_{k=k_1}^{k_1+r+1} c(k_1, k) f(u_{j+k}), \tag{3.17}$$

is used to represent the numerical flux. Here, r is the order of accuracy in L^∞ (i.e. the scheme is $(r+1)$th-order L^1), c is a constant matrix independent of $f(u)$ computed only once and stored, and the leftmost point location k_1 is decided locally by the ENO interpolation procedure (the precise formulae and the exact procedure are detailed in Shu *et al*. 1992). Upwinding is used in this stencil choosing process.

With an explict ENO scheme, a multi-dimensional scalar equation is handled dimension by dimension. Each derivative is treated as one-dimensional in computational space, and the above algorithm is applied. For a system of multidimensional equations, a local characteristic decomposition is first performed to transform the equations into a decoupled set of multidimensional scalar equations whose unknowns are the Riemann invariants of the original system of equations (Shu *et al*. 1992). Derivatives of the Riemann invariants are computed according to the one-dimensional algorithm.

The ENO scheme treats the symmetry axis differently from the compact scheme algorithm. The point-value ENO procedure stores solution variables at the cell centres and computes fluxes at cell edges. The axis $r = 0$ is placed at a cell edge rather than at a cell centre. Therefore, the computational domain is extended to the other side of the axis and uses ghost points. Symmetry conditions are imposed on all the variables at the end of each iteration at the ghost points, except for the radial and tangential velocities which are antisymmetric about $r = 0$.

4. Linear analysis

This section examines the linearized Euler and Rankine–Hugoniot (R-H) conditions with a view to obtaining some analytical and physical insight into the behaviour of the flow. Consider a shock normal to the mean flow and label the upstream and

https://doi.org/10.1017/S0022112096004880 Published online by Cambridge University Press

downstream sides by subscripts 1 and 2, respectively. From the steady-state R-H conditions, one readily deduces the relations

$$\left.\begin{aligned} M_2^2 &= \frac{2+M_1^2(\gamma-1)}{2\gamma M_1^2-(\gamma-1)}, \\ \rho_{21}=\frac{\rho_2}{\rho_1} &= \frac{(\gamma+1)M_1^2}{2+M_1^2(\gamma-1)}, \\ \frac{P_2}{P_1} &= \frac{2\gamma M_1^2-(\gamma-1)}{\gamma+1} \end{aligned}\right\} \tag{4.1}$$

between mean upstream and downstream variables.

Now consider an infinitesimal perturbation wave (denoted by primes) superimposed on the mean flow, but not necessarily aligned with it. These perturbation velocities are decomposed normal and parallel to the mean shock position. This in turn induces a perturbation in the shock position and orientation. Together with an assumed shock shape given by

$$x = x_s(r,t), \tag{4.2}$$

and the introduction of a finite shock velocity into the R-H conditions, their linearization with respect to perturbation amplitude leads to a linear system of equations for the downstream variables. For simplicity, we set the upstream axial and radial perturbation velocity components, and the upstream perturbation entropy, to zero. Solving the linearized R-H conditions for the downstream perturbation variables yields

$$\frac{s_2'}{\gamma} = \Lambda_{12}\frac{p_1'}{\gamma P_1} + \Pi_1\frac{x_{s,t}}{c_1}, \tag{4.3}$$

$$\frac{p_2'}{\gamma P_2} = \Lambda_{22}\frac{p_1'}{\gamma P_1} + \Pi_2\frac{x_{s,t}}{c_1}, \tag{4.4}$$

$$\frac{u_{x2}'}{c_2} = \Lambda_{32}\frac{p_1'}{\gamma P_1} + \Pi_3\frac{x_{s,t}}{c_1}, \tag{4.5}$$

$$\frac{u_{r2}'}{c_2} = \Pi_4 x_{s,r}. \tag{4.6}$$

Here, $s_2' = p_2'/P_2 - \gamma\rho_2'/\rho_2$ is the downstream perturbation entropy.

The nomenclature for the matrix coefficients is taken from Chang (1957) where the general solution for arbitrary upstream disturbances was derived. With the previous definitions, the matrix coefficients are

$$\Lambda_{12} = +\frac{M_2^2}{1-M_2^2}\left\{(1-\rho_{21})[1+(\gamma-1)M_2^2] + \left[1-\rho_{21}^2\left(\frac{M_2}{M_1}\right)^2\right]\right\} < 0, \tag{4.7a}$$

$$\Lambda_{22} = -\frac{M_2^2}{1-M_2^2}\left\{(1-\rho_{21}) + (1-\frac{\rho_{21}}{M_1^2})[1+(\gamma-1)(1-\rho_{21})M_2^2]\right\} > 0, \tag{4.7b}$$

$$\Lambda_{32} = \frac{M_2^2}{M_1(1-M_2^2)}(1-\rho_{21})\{2+(\gamma-1)(1-\rho_{21})M_2^2\} < 0, \tag{4.7c}$$

$$\Pi_1 = (\gamma-1)\frac{(1-\rho_{21})^2}{\rho_{21}}M_2 > 0, \tag{4.7d}$$

https://doi.org/10.1017/S0022112096004880 Published online by Cambridge University Press

$$\Pi_2 = -\frac{M_2}{1-M_2^2}\,\frac{1-\rho_{21}}{\rho_{21}}\,[2+(\gamma-1)(1-\rho_{21})M_2^2] > 0, \tag{4.7e}$$

$$\Pi_3 = -\frac{1}{1-M_2^2}\,\frac{1-\rho_{21}}{\rho_{21}}\,[1+M_2^2+(\gamma-1)(1-\rho_{21})M_2^2] > 0, \tag{4.7f}$$

$$\Pi_4 = -M_2(\rho_{21}-1) < 0. \tag{4.7g}$$

The inequalities in the expressions above hold for the range of upstream Mach numbers $M_1 > 1$. Several conclusions can be drawn from (4.3)–(4.6). First, note that u'_θ is continuous across the shock, and is therefore absent from the linearized R-H relations. Second, u'_{r2} has the same radial profile as the shock slope $x_{s,r}(r,t)$. If the shock moves in the positive x-direction, then $x_{s,t} > 0$. In addition, if the shock velocity decreases away from the axis, then $x_{s,r} < 0$, which implies that $u'_{r2} > 0$. The sign of u'_{x2} is also positive since $p'_1 < 0$ in the upstream vortex core. Thus, if the shock is displaced in the upstream direction, its velocity is positive at the axis, and a counter-clockwise (in region $r > 0$) downstream vortex ring is generated. This vortex ring then convects downstream with the mean axial velocity U_2, while new vortex rings are continuously generated by the steady upstream. The final result is a perturbation velocity u'_{x2} pointing upstream at the axis, and pointing downstream at the top of the vortex ring. Superimposed on this ring of azimuthal vorticity is a downstream axial vortex characterized by the same azimuthal velocity distribution as upstream (to leading order), but with a lower relative (with respect to the downstream mean pressure) pressure variation within the vortex ($0.67 < \Lambda_{22} < 0.72$, for $1 < M_1 < \infty$). As expected, the signs of Λ_{12} and Π_1 are consistent with positive entropy generation across the shock.

5. Discussion of physical results

In this section, results from the S-F and ENO algorithms, as applied to the problem of shock/vortex interaction, are compared to the predictions of linear theory and to each other. Because of the low-order accuracy of ENO results in the vicinity of the shock, detailed verification of shock-related information is rather difficult. However, it is possible to verify results of the ENO scheme in the downstream region away from the shock where pointwise or integrated quantities can be checked. Therefore, after providing a mutual verification of the S-F method and linear theory in the linear regime, we use the S-F results to establish the limitations of linear theory. Then we use the S-F results to validate the ENO results for moderately strong vortices, especially with reference to the structure of the flow away from the shock. Finally we venture with the ENO scheme into the highly nonlinear regime of stronger vortices, which cannot be handled by the S-F method.

5.1. *Linear regime*

The validity and accuracy of the S-F algorithm have been verified in numerous situations involving plane acoustic, shear or entropy waves (Zang *et al*. 1984; Lasseigne *et al*. 1991). We consider specifically axial vortices 2.6 with strengths in the range $\epsilon \in [10^{-3}, 3]$ interacting with a Mach 2 shock. After the downstream solution computed by the S-F method has evolved for a fixed period of time, the downstream values of field and thermodynamic variables at the shock are compared to the corresponding predicted values obtained from the linear equations (4.3)–(4.6) using the upstream values and the computed shock speed at the particular instance in time.

We compute the error (both absolute (a.e.) and relative (r.e.)) for entropy, pressure

https://doi.org/10.1017/S0022112096004880 Published online by Cambridge University Press

ϵ	1	0.1	0.01	0.001
τ	0.067	0.0067	0.00067	0.000067
S (a.e.)	5.8×10^{-5}	5.8×10^{-9}	9.1×10^{-13}	2.1×10^{-14}
S (r.e.)	2.4×10^{-2}	2.4×10^{-4}	3.7×10^{-6}	8.5×10^{-6}
p (a.e.)	5.3×10^{-4}	5.1×10^{-8}	2.7×10^{-12}	7.8×10^{-14}
p (r.e.)	4.9×10^{-3}	4.6×10^{-5}	2.5×10^{-7}	7.0×10^{-7}
u_n (a.e.)	6.0×10^{-5}	6.1×10^{-9}	9.1×10^{-13}	3.1×10^{-15}
u_n (r.e.)	1.3×10^{-2}	1.4×10^{-4}	2.1×10^{-6}	7.2×10^{-7}

TABLE 1. Error of downstream variables at the shock between S-F and linear theory. Error is computed on the symmetry axis. Both absolute (a.e.) and relative errors (r.e.) are shown.

ϵ	3	2	1	0.1
τ	0.2018	0.1345	0.06726	0.006726
Entropy S	24.05%	9.95%	2.37%	0.024%
Pressure p	4.38%	1.90%	0.49%	0.005%
Velocity u_n	13.17%	5.69%	1.33%	0.014%

TABLE 2. Relative error of downstream variables at the shock between S-F and linear theory. Error is computed on the symmetry axis.

and velocity normal to the shock. A grid resolution of 50×150 and a downstream domain $x \in [1, \pi]$ ensured that the numerical errors did not contaminate the measured errors. Results at the symmetry axis (where the maximum error is found to occur) are presented in tables 1 and 2. As expected, the linear theory prediction is found to be accurate and match the S-F results in the range of vortex strength $\epsilon < 1$ ($\tau < 0.067$).

Since the perturbation $p_1' = O(\epsilon^2)$, $u_{1x}' = 0$, and u_θ' is continuous across the shock, it follows that all downstream perturbation variables are $O(\epsilon^2)$. The absence of $O(\epsilon)$ terms implies that the absolute error is $O(\epsilon^4)$ in the linear regime, and the relative error is $O(\epsilon^2)$. These results are clearly confirmed in table 1, except for simulations where absolute errors reach the roundoff error of the computer ($< 10^{-13}$).

As evidenced by the results from table 2, nonlinear effects become significant (relative errors greater than 1%) when $\epsilon M_1 > O(1)$. Note that for $\epsilon = 3$ ($\tau = 0.2$) the relative error between the linear theory prediction and the S-F computation is already 24% for entropy, suggesting strong nonlinear effects. The data also suggest that pressure is less affected by high ϵ than are entropy and normal velocity. Results in table 2 also suggest that for $\epsilon = 2$ and beyond, cubic nonlinearities seem to come into play because the relative error is growing slightly faster than quadratically with the vortex strength. Note that at $M_1 = 2$, flow reversal occurs at $\epsilon \approx 3.7$ which is beyond the nonlinear threshold (see §5.2). In all the cases considered, the linear results underestimate the magnitude of the nonlinearly computed perturbations of s_2', p_2', and u_{2x}'.

After the successful comparison between linear theory and S-F results, we compute the shock/vortex interaction with ENO and S-F schemes and compare the solutions in the downstream domain when $M_1 = 2$ and $\epsilon = 2$. We initialize the vortex according to IC-c (2.11) with $\alpha = 2$, and $\beta = 6$. The shock is initially located at $x = 0$. For the S-F simulation, the upstream domain extends to $x = 8$, and the downstream domain extends to $x = -10$, with the buffer domain starting at $x = -9$. Parallel to the shock,

https://doi.org/10.1017/S0022112096004880 Published online by Cambridge University Press

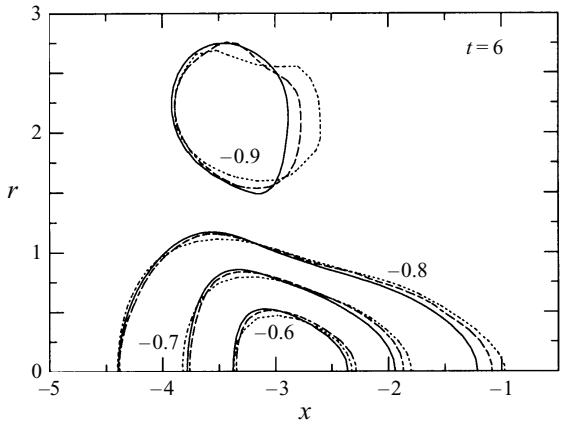


FIGURE 2. Superposition of ENO and S-F in the region $x \in [-5, 0]$, $r \in [0, 3]$. Contour levels of u_x range from -0.9 to -0.6 by increments of 0.1. Solid lines: S-F; dashed lines: ENO with 200×100 resolution; dotted lines: ENO with 100×50 resolution.

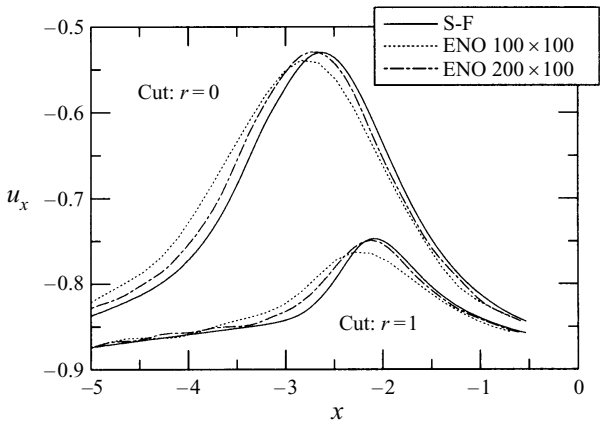


FIGURE 3. Cut of figure 2 at $r = 0$ and $r = 1$.

the grid stretching parameters are $A = 2.5$, $r_{max} = 20$ (see (3.8)). In computational space, the grid is uniform in both upstream and downstream domains, but with different grid spacings in the two domains. There are 60 axial grid points in the upstream domain. Coarse (100×48) and fine (200×96) downstream grids produce almost identical contour plots of u'_x, indicating a reasonably converged solution.

Conditions for the ENO scheme are as follows. The physical domain is defined by the region $x \in [-10, 8]$ and $r \in [0, 5]$, with a uniform grid in both directions. Coarse and fine resolution grid densities are 100×50 and 200×100, respectively. Although the results from the two algorithms were compared at various times, we present only the results at $t = 6$.

Figure 2 compares contour plots of axial velocity obtained from ENO and S-F in the region $x \in [-5, -1]$ and $r \in [0, 3]$. There are four equally spaced contour levels ranging from -0.9 to -0.6, with a maximum of -0.53 near $x = -3.0$. With a free-stream velocity $U_2 = -0.887$, the flow has not yet reversed. (The flow in the downstream domain is defined to have suffered reversal, i.e. incipient vortex breakdown, if the axial velocity points upstream at least at one point.) According to

https://doi.org/10.1017/S0022112096004880 Published online by Cambridge University Press

table 3, the circulation must approach the value 4 for breakdown to take place. The solid line represents the S-F results which may be considered as converged solutions. As expected, the ENO solution approaches the S-F solution as the grid is refined. When the axial grid resolution is doubled, the ENO contours lie approximately half way between the S-F contours and the ENO contours with a coarser grid. Cuts through the contours of figure 2 at $r = 0$ and $r = 1$ are shown in figure 3 to quantify the differences between the solutions. The refined ENO solution is approximately half way between the coarse ENO and SF. This is consistent with a first-order-accurate solution. As explained by Casper & Carpenter (1996), the first-order accuracy is the result of the propagation of the first-order error near the shock through the downstream characteristics.

5.2. *Vortex breakdown regime*

The comparisons performed in the previous subsection demonstrate that linear theory accurately predicts the phenomena associated with the interaction of a shock wave with an axial vortex for the range of vortex circulations ϵ and shock Mach numbers M_1 such that $\epsilon M_1 < O(1)$. As the vortex strength is increased beyond this linear limit, the deceleration of the axial flow across the shock increases the likelihood of the vortex breaking down. This is best understood by considering the angle formed by the streamlines and the symmetry axis (referred to in the Introduction as the helix angle),

$$\Theta = \arctan \tau = \arctan \frac{u_{\theta max}}{u_\infty}, \tag{5.1}$$

where u_∞ is the free-stream axial velocity. This equation shows that Θ increases if either u_∞ decreases (stronger shock), or $u_{\theta max}$ increases (stronger vortex). In the case of the incompressible axisymmetric vortex, it is known that breakdown is highly probable when Θ reaches a critical value around 57° (Spall *et al*. 1987). Experiments (Cattafesta 1992; Délery *et al*. 1984), and numerical simulations (Délery *et al*. 1984) indicate that the vortex strength τ required to induce flow reversal downstream of the shock decreases with increasing Mach number. We are interested in reproducing these results with an accurate time-dependent simulation. Previous investigations assumed constant enthalpy for reasons of efficiency, thus assuming the existence of a steady-state solution (Délery *et al*. 1984).

Although both ENO and S-F are adequate to trace out the envelope of incipient breakdown, we opted to use ENO for expediency. Spot checks at $M_1 = 2$ and $M_1 = 5$ with S-F confirm the ENO results. The initial conditions used for this were IC-b.

The computational domain for ENO is $x \in [-4, 2]$, $r \in [0, 5]$, with a uniform grid of 100×75 points. A uniform axial vortex is placed in the upstream domain $x > 0$. For each shock Mach number, several runs are conducted with values of ϵ on either side of its critical value. We compute the maximum axial velocity in the downstream domain. If this value is greater than zero, we consider that the flow has reversed. In the absence of reversal, the minimum axial velocity eventually oscillates around a constant negative value, which we take as an indication that the solution has reached a quasi-steady state.

The results of the parametric study are recorded in table 3 and figure 4. Table 3 shows a range of Mach numbers from 1.3 to 10. The value of ϵ for which the incipient breakdown occurs is given in the second column, and is the average of the two numbers in the third column. These are the two closest values of ϵ we tested which are on each side of the breakdown curve. Clearly, determining the critical value of ϵ to arbitrary precision is naturally difficult and prohibitively expensive, as is the

https://doi.org/10.1017/S0022112096004880 Published online by Cambridge University Press

M_1	ϵ	Range of ϵ	τ
1.3	4.93	(4.90, 4.95)	0.510
1.5	4.53	(4.50, 4.55)	0.406
1.7	4.18	(4.15, 4.20)	0.331
2.0	3.78	(3.75, 3.80)	0.254
2.5	3.33	(3.30, 3.35)	0.179
3.0	3.02	(3.00, 3.03)	0.135
3.5	2.73	(2.70, 2.75)	0.105
4.0	2.64	(2.63, 2.65)	0.0888
4.5	2.51	(2.50, 2.51)	0.0750
5.0	2.51	(2.50, 2.51)	0.0675
6.0	2.28	(2.25, 2.30)	0.0511
7.0	2.18	(2.15, 2.20)	0.0419
8.0	2.16	(2.15, 2.16)	0.0363
9.0	2.11	(2.10, 2.12)	0.0315
10.0	2.08	(2.05, 2.10)	0.0280

TABLE 3. The vortex breakdown or flow reversal values.

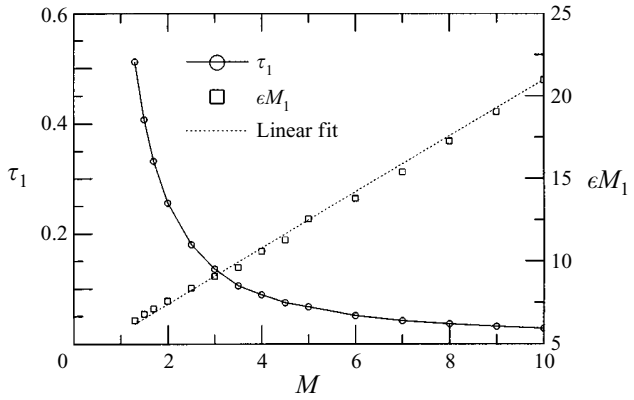


FIGURE 4. Plot of τ_1 and ϵM_1 versus Mach number for $M_1 \in [1.5, 10]$. Results based on ENO.

case with physical or numerical experiments. Several refined ENO simulations were performed on a 200×150 grid to confirm the results obtained on the coarser mesh.

The variation of $\tau = \tau_1$ versus Mach number is shown in figure 4. As expected, the upstream vortex strength necessary to initiate breakdown decreases with increasing Mach number. Intuitively, this makes sense since a stronger shock leads to a stronger deceleration of the axial flow, thus pushing the helix angle towards its critical value. An alternative way to quantify the relationship between shock and vortex strength is to plot the degree of nonlinearity of the shock–vortex interaction versus Mach number (figure 4). A linear curve fit is provided by the straight line

$$\epsilon M_1 = 1.7\, M_1 + 4.0 \tag{5.2}$$

over the range of $M_1 \in [1, 10]$. Equation (5.2) could serve as a practical curve for experimentalists and engineers.

As explained in Délery *et al*. (1984), the presence of the shock decelerates the mean upstream vortex thus increasing Θ. A rule of thumb for incompressible flow is that when Θ reaches 57°, the vortex is susceptible to an axisymmetric breakdown. A

https://doi.org/10.1017/S0022112096004880 Published online by Cambridge University Press

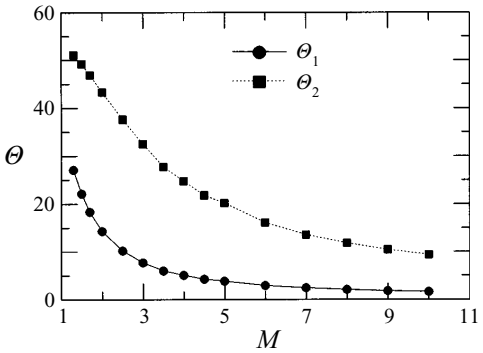


FIGURE 5. Θ_1 and Θ_2 versus Mach number.

simple model of vortex breakdown was given in Cattafesta (1992) who expressed the downstream τ_2 as a function of upstream quantities to obtain

$$\frac{\tau_2}{\tau_1} = \frac{u_{x1}}{u_{x2}} = \frac{\rho_{21}}{\rho_{21}\sin^2\psi + \cos^2\psi}, \tag{5.3}$$

where u_{xi}, $(i = 1, 2)$ are axial velocities upstream and downstream of the shock respectively, and ψ is the angle between the shock and the shock normal (figure 1). The density ratio across the shock is

$$\rho_{21} = \frac{(\gamma+1)M_1^2\cos^2\psi}{(\gamma-1)M_1^2\cos^2\psi + 1}. \tag{5.4}$$

Cattafesta (1992) assumed that the shock was normal ($\psi = 0°$) and determined a best constant value of τ_2 over the range of Mach numbers considered by Délery *et al.* (1984). This yielded $\tau_2 = 0.6$, or $\Theta_2 \approx 30°$ which is at variance with the critical $\Theta_2 = 57°$ for the incompressible vortex. Assuming that the incompressible limit for Θ_2 is reached at $M_1 = 1$ leads to the conclusion that the critical value of Θ_2 at which breakdown occurs is a function of the upstream shock Mach number. Therefore, we compute Θ_2 based on (5.3), with the values of τ_1 taken from table 3 to obtain the variation of Θ_2 with M_1 shown in figure 5. Note that the curve is approximately linear for $M_1 < 3.0$. Extrapolated to $M_1 = 1$, the Θ_2 curve predicts a critical angle $\Theta_2 = 55°$, consistent with incompressible results. In the limit $M_1 = 1$, the two curves must join, and $\Theta_1 = \Theta_2 \approx 55°$. At higher Mach numbers, the critical angle Θ_2 decreases down to 10°. Délery *et al.* (1984) obtained experimental points on the reversal curve for $M_1 = 1.7, 2.0, 2.3$. They obtained $\Theta_2 = 47°, 40°$ and 30.5°, respectively. Based on our observations relating the effects of the pressure core and the resulting shock motion, the discrepencies could be partially explained by an axial velocity deficit present in the experiments, but absent from the simulations.

If ϵ is increased beyond the point where the vortex breaks down, the shock eventually forms a triple point, with a more complicated structure in the recirculating region. This regime cannot be computed by the S-F code because of the appearance of internal shocks in the downstream domain and is now studied exclusively with the ENO algorithm.

5.3. *Shock bifurcation regime*

To complete the study of flow configurations as a function of vortex strength and shock Mach number, we perform ENO calculations for $\epsilon = 7$ and 9, at $M_1 = 2$ and 4.

https://doi.org/10.1017/S0022112096004880 Published online by Cambridge University Press

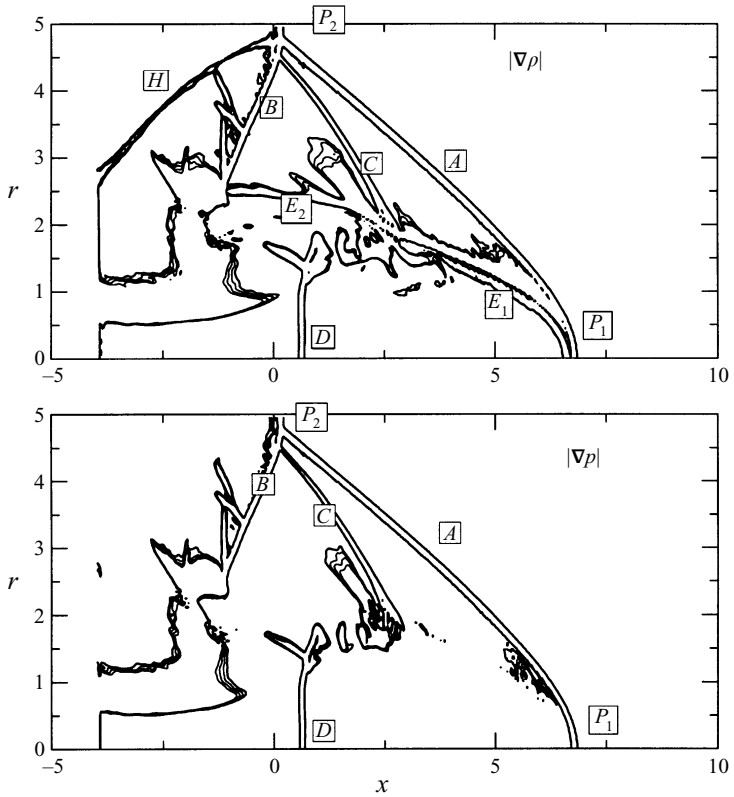


FIGURE 6. Schematic of flow configuration for a smooth start case at $t = 11$.

The physical domain extends from $x = -4$ to $x = 8$ in the axial direction, and to $r = 5$ radially. Grid resolution is 450×150. These parameter values were chosen to ensure the occurrence of a triple point in the shock, hereafter referred to as shock bifurcation. The triple point is expected to form at $r = O(1)$ since the vortex core radius is the only physical length scale in the problem. The chosen values of ϵ far exceed the breakdown criterion; the flow is highly nonlinear.

We consider two different set of initial conditions: IC-a and IC-c. Recall that IC-a refers to a vorticity profile and perturbation temperature constant across the upstream and downstream domains, whereas IC-c has zero vorticity downstream and an upstream vorticity multiplied by a spatial blending function (§2). The structure of the flow is a function of the initial conditions (compare figures 7 and 10).

Contour plots of $|\nabla\rho|$ and $|\nabla p|$ for a $M_1 = 2$, $\epsilon = 7$ flow with IC-c at $t = 11$ are shown in figure 6. For comparison, density contours are shown in figure 7. The gradient functions are normalized so that their maximum is unity. Contours in the range [0.03,0.04] are plotted. The choice of variables is consistent with the features visible in a typical schlieren photograph. The flow slip lines are easily identified from the features present in the density gradient contours and absent from the pressure gradient plot (E_1, E_2, and H in figure 6). The upstream pressure is minimum at the centre of the vortex core, and increases radially to its free-stream value. As the plane shock interacts with the vortex (at P_1), the local shock Mach number is higher in the core region than elsewhere. In other words, the shock bulges forward in the vicinity of the axis. As the obliqueness of the primary shock (A) increases, a local

https://doi.org/10.1017/S0022112096004880 Published online by Cambridge University Press

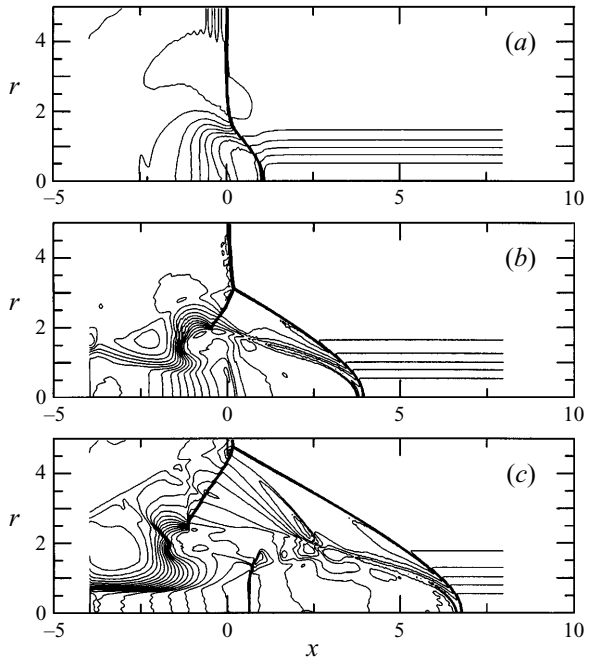


FIGURE 7. Time history (*a*) $t = 3$, (*b*) 7, (*c*) 11 of density. Computed with ENO, $M_1 = 2$, $\epsilon = 7$. Smooth start: $x \in [2, 6]$. Initial conditions IC-c.

region of supersonic flow eventually forms downstream of (A), necessarily terminated by another shock (B) to match with the downstream subsonic flow, thus forming a lambda shock with the so-called triple point (P_2). Another weak shock (C) is evident in the supersonic region, between shocks (A) and (B). The slip lines (E_1) and (E_2) are separated by the foot of the shock (C), and they coincide with the unit-Mach-number (sonic) contour line which emanates from the point of intersection (P_1) of the primary shock (A) with the axis of symmetry. Thus, the supersonic region is delimited by the shocks (A), (B) and the sonic lines (E_1) and (E_2). As the primary shock (A) begins to move upstream in the region near the axis, a counterclockwise azimuthal vortex ring is formed. This vortex ring has an elliptical cross-section in the (x, r)-plane. Its major axis slowly rotates counterclockwise, and moves steadily away from the axis $r = 0$. As the flow turns supersonically within the vortex (figure 8), it is decelerated through the shocks (B) and the triple-point structure at the tip of the normal shock (D). The velocity vectors near the axis in figure 8 suggest a structure analogous to that of an expanding nozzle with a shock consistent with subsonic exit conditions.

Figure 7 shows density contour plots at $t = 3, 7, 11$ for the IC-c, with a spatial ramp function defined by (2.11) ($\alpha = 2$, $\beta = 6$). Although we do not present the results here, we have also simulated the abrupt start case defined by IC-b, and find that the results are qualitatively similar to figure 7, but with a time shift. Figure 7(*a*) ($t = 3$) shows the density prior to the formation of the triple point. The triple point forms around $t = 4$. By $t = 7$, the triple-point shock configuration is well formed (figure 7*b*), and as evidenced by figure 7(*c*) at $t = 11$, this formation seems to evolve self-similarly. The structure of the flow in the recirculating region is presented in figure 8 in which vector plots of the flow in the (x, r)-plane are superimposed on contours of Mach number (based on v_x and v_r). The contour values range from 0 to 2.5 in increments of

https://doi.org/10.1017/S0022112096004880 Published online by Cambridge University Press

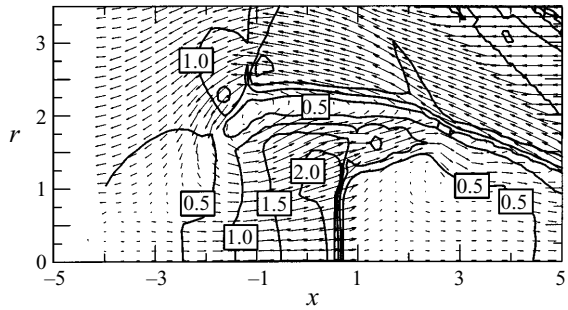


FIGURE 8. Velocity vector plots in the (x, r)-plane, superimposed on contours of Mach number (projected in the x, r-plane). Contours are at intervals of 0.5. The vectors are plotted every 10 points in x and every 4 points in r.

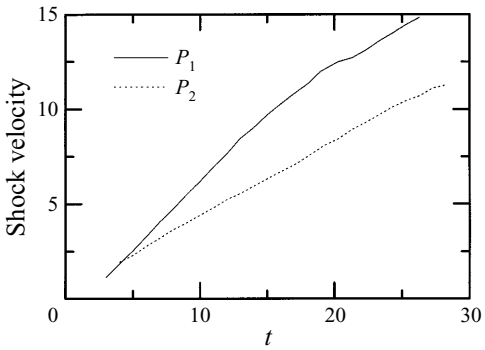


FIGURE 9. Position of P_1 and P_2 as a function of time. The initial data and grid are given in the text.

0.5. The results are shown at $t = 11$. As the flow begins to wrap around the subsonic region (bounded by the sonic lines E_1, E_2, the shock D, and the symmetry line), it decelerates, and becomes subsonic. At this point, the flow reaccelerates, eventually becomes supersonic, and is eventually slowed down by passage through a normal $M_1 = 2$ shock (D).

To test whether the flow maintains its self-similar motion for longer time periods, we first coarsened the grid to 100×50 on the same physical domain and compare the primary shock structure to the finer grid results of figure 7. We find, as expected, that the coarseness of the grid does not modify the characteristics of the downstream flow (even at $t = 11$ where the triple point is very close to the upper boundary of the physical domain). Therefore, we increased the size of the physical domain to $x \in [-9, 15]$, $r \in [0, 12]$, and ran the simulation to $t = 28$. At this late stage, the structure of the primary and secondary shocks is still the same as for $t = 11$, but spatially enlarged. We track the position of P_1 (the point of intersection of the shock and the axis) and P_2 (the shock triple point) and find that P_2 is moving at a constant velocity towards the free stream (figure 9). On the other hand, the speed of P_1 seems to slow down as it moves upstream. These results suggest the possibility of a theoretical framework within which a self-similar flow emerges for particular combinations of the parameters M_1 and ϵ.

In contrast to results with the initial conditions IC-c, figure 10(*a–c*) shows the time evolution of the density for case IC-a, where a vortex is superimposed initially on a

https://doi.org/10.1017/S0022112096004880 Published online by Cambridge University Press

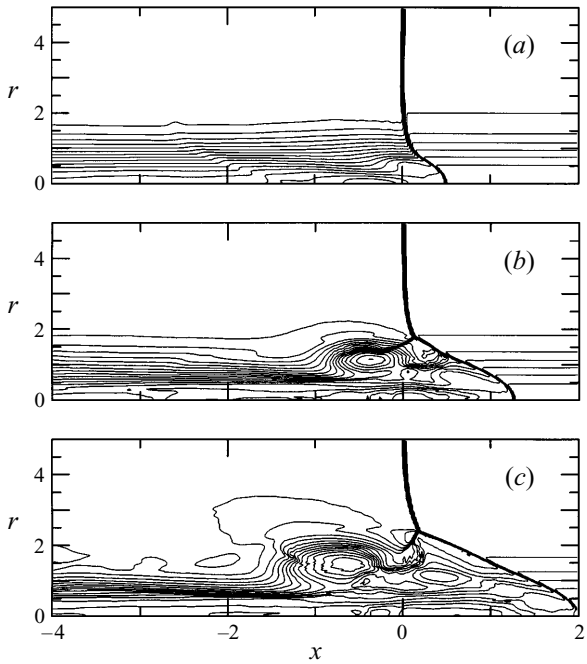


FIGURE 10. Time history (*a*) $t = 3$, (*b*) 7, (*c*) 11 of density. Computed with ENO, $M_1 = 2$, $\epsilon = 7$. (Initial conditions IC-a.)

shocked uniform flow. The evolution appears to be self-similar, somewhat like that in figure 7, but evolves on a slower time scale. Rough velocity measurements of points P_1 and P_2 between $t = 7$ and $t = 11$ indicate that for IC-a, P_1 moves approximately 3.5 times slower, and P_2 moves about 2.5 times slower, than the corresponding points of case IC-c. This indicates that the shock is more oblique when the vortex interacts with the shock abruptly. A physical explanation is offered by considering the initial pressure jump across the shock, which for our choice of parameters is about twice as strong in case IC-b. This indicates that case IC-b generates a shock with stronger acceleration into the upstream domain near the symmetry axis.

Once the triple point is formed and starts to move towards the free stream, what is its ultimate destiny? Does it continue to move at a constant velocity, or does it slow down, and eventually stop, setting the stage for a possible steady-state solution? We try to answer this question by appealing to dimensional analysis. The physical parameters that govern this problem are the mean upstream velocity U_1, the upstream mean sound speed c_1, the normalized vortex strength $\epsilon = \Gamma\gamma^{1/2}/(r_0 c^*)$, the vortex core radius r_0, the spatial coordinates x^* and c^*, and time t^*. (An asterisk denotes dimensional quantities.) The downstream velocity field therefore takes the general form

$$u_i'(x^*, y^*, t^*) = c^* f\left(M_1, \epsilon, \frac{x^*}{r_0}, \frac{y^*}{r_0}, \frac{c_1 t^*}{r_0}\right). \tag{5.5}$$

In the limit of vanishing core radius, or equivalently, as $t^*/(c_1 r_0) \to \infty$, the velocity field must take the self-similar form

$$u_i'\left(\frac{x^*}{t^*}, \frac{y^*}{t^*}\right) = c^* f\left(M_1, \epsilon, \frac{x^*}{c_1 t^*}, \frac{y^*}{c_1 t^*}\right). \tag{5.6}$$

https://doi.org/10.1017/S0022112096004880 Published online by Cambridge University Press

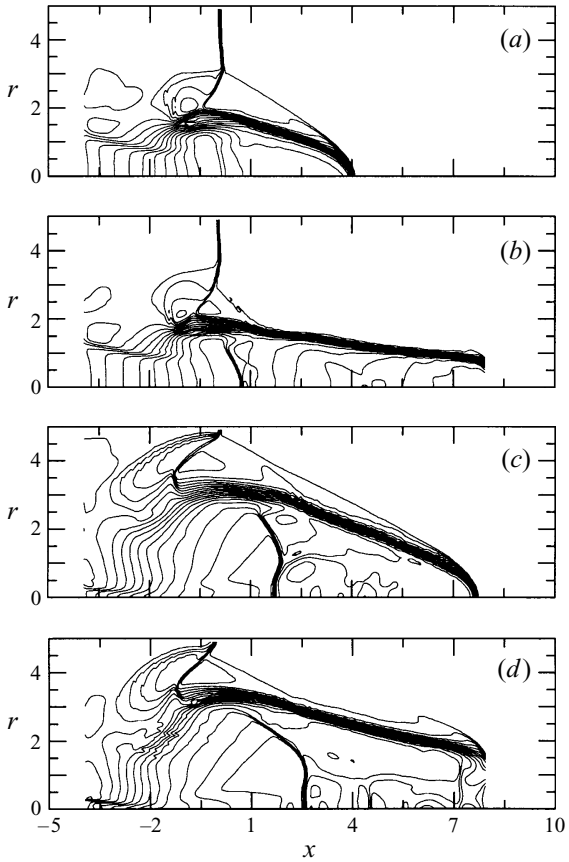


FIGURE 11. Streamwise velocity contours at $t = 7$ for (*a*) $M_1 = 2$, $\epsilon = 7$, (*b*) $M_1 = 2$, $\epsilon = 9$, (*c*) $M_1 = 4$, $\epsilon = 7$, and (*d*) $M_1 = 4$, $\epsilon = 9$.

Expressions for the velocity of the triple point P_2 and that of the intersection of the primary shock and the axis (P_1) are easily obtained from (5.5) by suppressing the dependence on the spatial coordinates:

$$v_{P_i} = c_1 f\left(M_1, \epsilon, \frac{c_1 t^*}{r_0}\right) \tag{5.7}$$

which implies a constant velocity as the third argument becomes very large. Of course, this velocity might be zero.

Numerical results seem to indicate that there is a region of (ϵ, M_1) parameter space for which the function f is independent of time. However that need not be the case. A theoretical study of this matter would prove most interesting. For example, what is the structure of f as $t \to \infty$, $\Gamma \to \infty$, or $M_1 \to \infty$? Intuitively, one could argue that once out of range of the upstream vortex filament, having reached a constant velocity, the triple point would continue on forever. Given the assumption that the point P_2 moves at constant velocity, a slowdown of the triple point would increase the obliqueness of the shock, eventually leading to its breakdown. Simulations at higher values of ϵ have led to shock breakdown.

To understand better the effect of M_1 and ϵ on the triple-point motion, we perform and display results at $M_1 = 2$ and 4, for $\epsilon = 7$ and 9. These are presented in figure 11.

https://doi.org/10.1017/S0022112096004880 Published online by Cambridge University Press

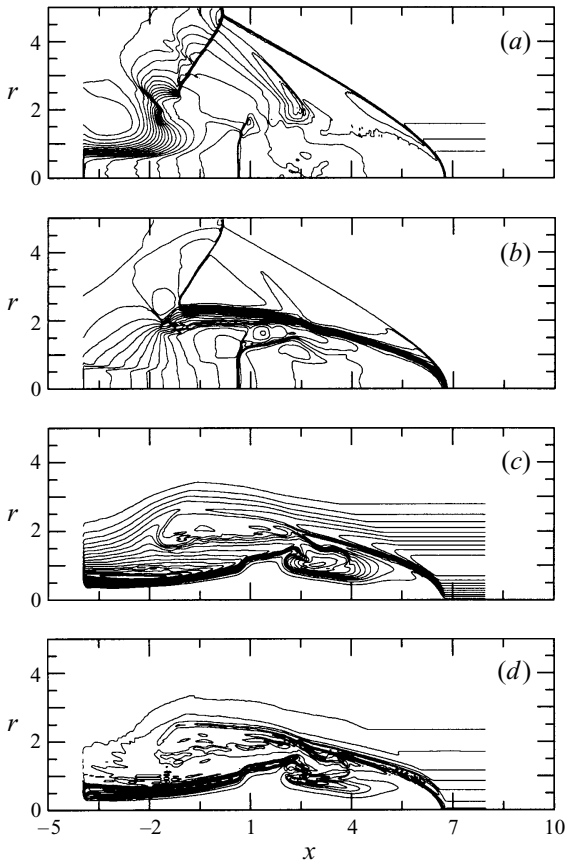


FIGURE 12. Plots of (*a*) p, (*b*) u_x, (*c*) u_θ and (*d*) ω_x at $t = 11$. Computed with ENO, $M_1 = 2$, $\epsilon = 7$. Initial conditions IC-c. Smooth start: $x \in [2, 6]$.

Comparing figures 11(*a*) ($M_1 = 2, \epsilon = 7$) and 11(*b*) ($M_1 = 2, \epsilon = 9$), one sees that the velocity of the triple point P_2 (figure 6) does not depend on the vortex strength. However, P_1 moves at a much faster rate as ϵ is increased. This is consistent with a lower vortex core pressure, and thus a greater shock velocity near the axis. These results also hold for $M_1 = 4$ at the same values of ϵ (figure 11 *c*, *d*). On the other hand, the velocity of both P_1 and P_2 increases with Mach number.

These results allow us to draw some conclusions relating to the form of (5.7). The lack of dependence of v_{P_2} on ϵ implies that

$$v_{P_2} = c_1 f\left(M_1, \frac{c_1 t^*}{r_0}\right), \tag{5.8}$$

which is only a function of Mach number when the velocity is independent of time (i.e. $r_0 \to 0$). On the other hand, v_{P_1} retains the general form (5.7).

Now consider the limit as $M_1 \to \infty$ for which either $c_1 \to 0$ or $u_1 \to \infty$. We consider both cases. But first, consider the radial temperature profile. If one assumes that the entire vortex is isentropic, (2.6) implies that

$$T(r) = T_1 - \alpha^2(r)\epsilon^2 \tag{5.9}$$

where $\alpha(r)$ is a positive function and $\alpha(\infty) = 0$. Therefore, the Mach number in the

https://doi.org/10.1017/S0022112096004880 Published online by Cambridge University Press

vortex core is higher than in the free stream. Its radial profile is

$$M^2(r) = \frac{U_1^2}{c_1^2 - \alpha^2(r)\gamma\epsilon^2} \tag{5.10}$$

which gives a ratio of core to free stream Mach number

$$\frac{M_0}{M_1} = \frac{1}{(1 - \alpha^2(0)\gamma\epsilon^2/c_1^2)^{1/2}}. \tag{5.11}$$

If $U_1 \to \infty$, $M_0/M_1 = f(\epsilon, c_1)$ with $\epsilon < c_1/(\alpha(0)\gamma^{1/2})$ to ensure a positive core temperature. Therefore, the Mach number and vortex strength are independent parameters. If, on the other hand, $c_1 \to 0$, the ratio M_0/M_1 is still given by (5.11), except that the maximum vortex strength decreases proportionally to c_1. In this case, one cannot take the limit $M_1 \to \infty$ while keeping ϵ fixed. In other words, the aforementioned expressions for the triple points, and their 'self-similar' properties, are found for increasingly weaker vortices as the Mach number is increased by decreasing c_1.

Combining the above statements, as $M_1 \to \infty$ ($c_1 \to 0$) the velocities of P_1 and P_2 satisfy either $v_{P_i} = U_1 f(\epsilon, U_1 t^*/r_0)$ or $v_{P_i} = c_1 f(\epsilon, U_1 t^*/r_0)$. In the latter case, the velocity drops to zero in the limit $M_1 \to \infty$. We assume that ϵ is kept fixed as $c_1 \to 0$, e.g. by decreasing the vortex circulation. Since $\epsilon < O(c_1)$, one must have $\Gamma < O(c_1^2)$.

When $M_1 \to \infty$ ($U_1 \to \infty$), $v_{P_i} = c_1 f(\epsilon, c_1 t^*/r_0)$, which implies that the triple point has a velocity $v_{P_2} = c_1 f(\epsilon, c_1 t^*/r_0)$.

In the above discussion, we have assumed that the generic function $f(\cdots)$ remained finite as its various limits were taken. If the time argument becomes infinite and if $f(\cdots)$ remains bounded, $f(\cdots)$ can (in principle) take an oscillatory form. This might correspond to the periodic shedding of downstream vortices. In the event $f(\cdots)$ is unbounded, more general forms must be considered.

Figure 12(*a*)–12(*d*) show the solution of the IC-c case at $t = 11$ for p, u_x, u_θ, and axial vorticity w_x ($M_1 = 2, \epsilon = 7$). An 'airfoil'-like structure is apparent in figure 12(*b*). This region acts as a fictitious solid body around which the flow rapidly accelerates (figure 12*c*). If the acceleration is sufficiently strong, the flow becomes supersonic as it redirects itself in the upstream direction. To adjust back to the subsonic field adjacent to the primary shock, a secondary shock is formed at the axis (*D* in figure 6). The secondary shock forms an almost perfect normal Mach disk. The axial location of this shock is approximately steady and has a Mach number of 1.34. As expected, the axial vorticity is continuous across the shock, but has strong variations inside the 'airfoil'. This is consistent with strong variations of v_θ in this region.

6. Concluding remarks

In this paper, we have studied the interaction of a shock with a longitudinal isentropic vortex over a wide range of Mach numbers and vortex strengths. Three regimes are brought to light. In the first, the vortex strength ϵ satisfies $\epsilon M < 1$, in which case linear results are valid. As ϵ increases, the nonlinear effects emerge. First, a flow reversal occurs downstream of the shock, accompanied by a vortex breakdown. This effect is primarily due to the deceleration of the mean flow across the shock, which increases the helicity of the vortex, thus eventually leading to its breakdown. We determined numerically ϵ as a function of the Mach number for which incipient vortex breakdown occurs. When the ordinate is expressed as ϵM, this curve becomes

https://doi.org/10.1017/S0022112096004880 Published online by Cambridge University Press

approximately linear, particularly at the higher Mach numbers. As ϵ is increased even further, the resulting obliqueness of the shock leads to a supersonic pocket in the downstream region which readjusts to subsonic conditions through a secondary shock emanating from the primary shock at the so-called triple point. A parameter study in this range of vortex strengths using ENO uncovered a regime in which the motion of the triple point and of the point of intersection of the primary shock with the axis of symmetry looks self-similar. Further study uncovered a regime in which the triple-point velocity, normalized by c_1, was only a function of the shock Mach number. Under extreme conditions, the shock can even break, when a supersonic upstream flow can no longer be maintained. This is due to the strong Mach number gradient between the vortex core and its edge. This condition is easiest to reach for relatively weak shocks. Currently, there are no nonlinear theories to explain these results. Theoretical developments, particularly those based on self-similar notions, might go a long way towards understanding in more detail some of the mechanisms described herein.

The authors would like to thank M. Carpenter, S. Berger, K. Meadows, and S. Woodruff for exciting discussions. This work was supported by NASA Contract NAS1-19480 while the first two authors were in residence at ICASE. The third author was also supported by ARO grant DAAH04-94-G-0205, NSF grant DMS-9500814, NASA grant NAG1-1145, and AFOSR grant 95-1-0074.

REFERENCES

Canuto, C., Hussaini, M. Y., Quarteroni, A. & Zang, T. A. 1987 *Spectral Methods in Fluid Dynamics*. Springer.

Carpenter, M. H., Gottlieb, D. & Abarbanel, S. 1993 The stability of numerical boundary treatments for compact high-order finite-difference schemes. *J. Comput. Phys.* **108**, 272–295.

Carpenter, M. H. & Kennedy, C. A. 1994 Fourth-order 2N-storage Runge–Kutta schemes. *NASA-TM*-109112.

Casper, J. & Carpenter, M. H. 1996 Computational considerations for the simulation of shock-induced sound. *NASA-TM*-110222.

Cattafesta, L. N. III 1992 An experimental investigation of shock wave/vortex interaction. PhD Thesis, Penn. State University.

Cattafesta, L. N. III & Settles, G. S. 1992 Experiments on shock/vortex interactions. *AIAA Paper* 92-0315.

Chang, C. T. 1957 Interaction of a plane shock and oblique plane disturbances with special reference to entropy waves. *J. Aero. Sci.* **24**, 675–682.

Délery, J., Horowitz, E., Leuchter, O. & Solignac, J.-L. 1984 Fundamental studies on vortex flows. *La Recherche Aérospatiale*, No. 2, 1–24.

Dosanjh, D. S. & Weeks, T. M. 1965 Interaction of a starting vortex as well as a vortex street with a traveling shock wave. *AIAA J.* **3**, 216–223.

Ellzey, J. L., Henneke, M. R., Picone, J. M. & Oran, E. S. 1995 The interaction of a shock with a vortex: shock distortion and the production of acoustic waves. *Phys. Fluids* **1**, 172–184.

Erlebacher, G., Hussaini, M. Y. & Jackson, T. L. 1996 Nonlinear strong shock-vortex interactions: a shock-fitted approach *Theor. Comput. Fluid Dyn.* (Submitted).

Harten, A., Engquist, B., Osher, S. & Chakravarthy, S. 1987 Uniformly high order essentially non-oscillatory schemes, III. *J. Comput. Phys.* **71**, 231–303.

Hussaini, M. Y., Kopriva, D. A., Salas, M. D. & Zang, T. A. 1985 Spectral methods for the Euler equations II — Chebyshev methods and shock-fitting. *AIAA J.* **23**, 234–240.

Kopriva, D. A. 1988 A multidomain spectral collocation computation of the sound generated by a shock-vortex interaction. In *Computational Acoustics: Algorithms and Applications,* vol. 2 (ed. D. Lee & M. H. Schultz). Elsevier.

https://doi.org/10.1017/S0022112096004880 Published online by Cambridge University Press

Kopriva, D. A., Zang, T. A. & Hussaini, M. Y. 1991 Spectral methods for the Euler equations: the blunt body problem revisited. *AIAA J.* **9**, 1458–1462.

Lasseigne, D. G., Jackson, T. L. & Hussaini, M. Y. 1991 Nonlinear interaction of a detonation/vorticity wave. *Phys. Fluids* A **3**, 1972–1979.

Lele, S. K. 1992 Compact finite difference schemes with spectral-like resolution. *J. Comput. Phys.* **103**, 16–42.

McKenzie, J. F. & Westphal, K. O. 1968 Interaction of linear waves with oblique shock waves. *Phys. Fluids* **11**, 2350–2362.

Meadows, K. R. 1995 A numerical study of fundamental shock-noise mechanisms. PhD Dissertation, Cornell University.

Meadows, K. R., Kumar, A. & Hussaini, M. Y. 1991 Computational study on the interaction between a vortex and a shock wave. *AIAA J.* **29**, 174–179.

Naumann, A. & Hermanns, E. 1973 On the Interaction between a shock wave and a vortex field. *AGARD-CP*-131.

Pao, S. P. & Salas, M. D. 1981 A numerical study of two-dimensional shock-vortex interaction. *AIAA Paper*-81-1205.

Ribner, H. S. 1954 Convection of a pattern of vorticity through a shock wave. *NACA Rep.* 1164.

Ribner, H. S. 1986 Spectra of noise and amplified turbulence emanating from shock-turbulence interaction. *AIAA J.* **25**, 436–442.

Rizetta, D. P. 1995 Numerical simulation of oblique shock-wave/vortex interaction *AIAA J.* **33**, 1441–1446.

Shu, C.-W. & Osher, S. 1988 Efficient implementation of essentially non-oscillatory shock capturing schemes. *J. Comput. Phys.* **77**, 439–471.

Shu, C.-W. & Osher, S. 1989 Efficient implementation of essentially non-oscillatory shock-capturing schemes II. *J. Comput. Phys.* **83**, 32–78.

Shu, C.-W., Zang, T. A., Erlebacher, G., Whitaker, D. & Osher, S. 1992. High order ENO schemes applied to two and three dimensional compressible flow. *Appl. Numer. Maths* **9**, 45–71.

Spall, R. E., Gatski, T. B. & Grosch, C. E. 1987 A criterion for vortex breakdown. *Phys. Fluids* **30**, 3434–3440.

Ta'asan, S. & Nark, D. 1995 An absorbing buffer zone technique for acoustic wave propagation. *AIAA Paper*-95-0164.

Zang, T. A., Hussaini, M. Y. & Bushnell, D. M. 1984 Numerical computations of turbulence amplification in shock-wave interactions. *AIAA J.* **22**, 13–21.

https://doi.org/10.1017/S0022112096004880 Published online by Cambridge University Press